NANO · MICRO
small
www.small-journal.co

Golden Bristlegrass-Like Hierarchical Graphene Nanofibers Entangled with N-Doped CNTs Containing $CoSe_2$ Nanocrystals at Each Node as Anodes for High-Rate Sodium-Ion Batteries

*Min Su Jo, Jae Seob Lee, Sun Young Jeong, Jae Kwang Kim, Yun Chan Kang,**
Dong Won Kang, Sang Mun Jeong, and Jung Sang Cho**

Golden bristlegrass-like unique nanostructures comprising reduced graphene oxide (rGO) matrixed nanofibers entangled with bamboo-like N-doped carbon nanotubes (CNTs) containing $CoSe_2$ nanocrystals at each node (denoted as N-CNT/rGO/$CoSe_2$ NF) are designed as anodes for high-rate sodium-ion batteries (SIBs). Bamboo-like N-doped CNTs (N-CNTs) are successfully generated on the rGO matrixed nanofiber surface, between rGO sheets and mesopores, and interconnected chemically with homogeneously distributed rGO sheets. The defects in the N-CNTs formed by a simple etching process allow the complete phase conversion of Co into $CoSe_2$ through the efficient penetration of H_2Se gas inside the CNT walls. The N-CNTs bridge the vertical defects for electron transfer in the rGO sheet layers and increase the distance between the rGO sheets during cycles. The discharge capacity of N-CNT/rGO/$CoSe_2$ NF after the 10 000th cycle at an extremely high current density of 10 A g^{-1} is 264 mA h g^{-1}, and the capacity retention measured at the 100th cycle is 89%. N-CNT/rGO/$CoSe_2$ NF has final discharge capacities of 395, 363, 328, 304, 283, 263, 246, 223, 197, 171, and 151 mA h g^{-1} at current densities of 1, 2, 4, 6, 8, 10, 12, 14, 16, 18, and 20 A g^{-1}, respectively.

1. Introduction

Recently, transition-metal chalcogenides (TMCs) have widely been studied as anode materials for sodium-ion batteries (SIBs) because of their structural characteristics and unusual chemical, physical, and electronic properties.[1–3] However, their practical energy-storage performance is far below the expectations, mainly owing to their rapid capacity degradation even at low current rates, poor cycling stability, and intrinsic low conductivity, which greatly hinder the application of TMC materials in SIBs.[4–8] To solve these problems, TMC/carbon (C) hybrids with both optimum compositions and sophisticated-designed structures, such as FeS_2@C yolk–shell nanoboxes,[4] C/$MoTe_2$ core–shell microspheres,[5] multiroom-structured TMC/C microspheres,[6] $FeSe_2$/C microrods,[7] and fullerene-like $MoSe_2$/CNT balls,[8] have been investigated.

With regard to the TMC/C hybrid strategy, as representative conductive C materials, 1D carbon nanotubes (CNTs) and 2D graphene have attracted considerable attention in the field of energy storage owing to their unique properties, including their high electrical conductivities, large surface areas, and chemical and thermal stability.[9,10] This strategy goes further, a few studies on hybrid energy-storage materials comprising CNTs, graphene sheets, and TMCs have recently been performed to obtain synergistic effects of different C materials.[11–13] In general, graphene has low conductivity in the vertical direction despite its high electrical conductivity, and it easily forms irreversible agglomerates through van der Waals interactions.[14,15] However, to obtain anodes with high rate performance, it is

---

M. S. Jo, J. S. Lee, S. Y. Jeong, Prof. J. S. Cho
Department of Engineering Chemistry
Chungbuk National University
1, Chungdae-Ro, Seowon-Gu, Cheongju-Si, Chungbuk 28644,
Republic of Korea
E-mail: jscho@cbnu.ac.kr

Prof. J. K. Kim
Department of Solar & Energy Engineering
Cheongju University
298, Daeseong-Ro, Cheongwon-Gu, Cheongju-Si, Chungbuk 28503,
Republic of Korea

The ORCID identification number(s) for the author(s) of this article can be found under https://doi.org/10.1002/smll.202003391.

DOI: 10.1002/smll.202003391

Prof. Y. C. Kang
Department of Materials Science and Engineering
Korea University
145, Anam-Ro, Seongbuk-Gu, Seoul 02841, Republic of Korea
E-mail: yckang@korea.ac.kr

Prof. D. W. Kang
School of Energy Systems Engineering
Chung-Ang University
84, Heukseok-Ro, Dongjak-Gu, Seoul 06974, Republic of Korea

Prof. S. M. Jeong
Department of Chemical Engineering
Chungbuk National University
1, Chungdae-Ro, Seowon-Gu, Cheongju-Si, Chungbuk 28644,
Republic of Korea
E-mail: smjeong@cbnu.ac.kr

important to exploit the entire graphene layer—which provides favorable sites for energy storage—and to construct the overall conductivity of the graphene networks. In this regard, CNTs can bridge the vertical defects for electron transfer in the graphene layers and increase the distance between graphene sheets.[16,17] Therefore, when CNTs and graphene are combined with TMCs, synergistic effects on the anodes, such as improved cycle and rate capabilities, are expected, owing to the electron transport through the CNTs in the vertical direction facilitated by the bridging graphene and the suppression of the restacking of graphene sheets during repeated charge and discharge processes.[18,19]

Over the past few years, a few nanostructuring strategies using solvothermal, hydrothermal self-assembly, and spray pyrolysis processes have been employed to prepare TMCs/CNT/graphene multi-hybrids as anodes for SIBs.[20–22] For example, Yang et al. synthesized a WS_2/CNT/graphene aerogel via a solvothermal method followed by freeze-drying and post-annealing. The product exhibited a specific capacity of 253 mA h g^{-1} at a current density of 200 mA g^{-1} after 100th cycles.[20] An SnS_2/CNT/graphene aerogel was prepared by Kim et al. using hydrothermal self-assembly followed by a sulfidation process. The composite exhibited a reversible capacity of 536 mA h g^{-1} after 1000th cycles at 0.2 A g^{-1} and a rate capability of 304.8 mA h g^{-1} at a current density of 10 A g^{-1}.[21] Additionally, porous $MoSe_2$/CNT/graphene powders were synthesized using spray pyrolysis by Kang et al. The powders exhibited a discharge capacity of 335 mA h g^{-1} at 1 A g^{-1} after 400th cycles.[22] However, thus far, the long-term cycle and high-rate properties of TMCs/CNT/graphene multi-hybrids are unsatisfactory for practical applications owing to their intrinsic low structural stability and the polarization caused by slow sodium-ion diffusion.[23,24] Thus, it is necessary to develop more elaborately designed nanostructures of anodes for high-performance SIBs. To the best of our knowledge, well-developed CNTs that are chemically interconnected between graphene matrixed 1D structure with TMC nanoparticles are remains still a challenge and have not been studied.

In this study, we introduced a golden bristlegrass-like unique nanostructure comprising graphene matrixed nanofibers entangled with bamboo-like N-doped CNTs (N-CNTs) containing $CoSe_2$ nanocrystals at each node for the first time as high-rate anodes for SIBs. Bamboo-like N-CNTs were successfully generated both on the graphene matrixed nanofiber surface and as bridges between the graphene sheets and mesopores formed by polystyrene (PS) decomposition, and they were chemically interconnected with homogeneously distributed graphene sheets with the help of dicyandiamide (DCDA), which was a source of both C and N. In particular, it is very difficult to perform selenization of Co nanocrystals trapped inside a CNT wall, because the H_2Se gas for selenization cannot penetrate the thick CNT wall; however, $CoSe_2$ was successfully generated in this study. By partially introducing defects into the CNT walls during the intermediate heat treatment, the gas-diffusion process, and phase conversion of Co were easily achieved. Additionally, the CNTs were doped with N, which was promising for improving the electrical conductivity of the cell.

The detailed formation mechanism of the hierarchical graphene nanofibers entangled with bamboo-like N-CNTs containing $CoSe_2$ nanocrystals was investigated by tracing the morphologies and crystal structures of the samples obtained at each step. Moreover, the electrochemical performance of the unique nanostructure for sodium-ion storage was compared with that of bare filled-structure $CoSe_2$ nanofibers.

2. Results and Discussion

The golden bristlegrass-like graphene matrixed nanofibers entangled with bamboo-like N-CNTs containing $CoSe_2$ nanocrystals at each node (N-CNT/rGO/$CoSe_2$ NF) were prepared by applying a multi-step heat-treatment process to the electrospun nanofibers. The detailed formation mechanism for the unique nanostructure is described in **Scheme 1**. The precursor nanofibers uniformly composed of Co salt, poly(vinyl alcohol) (PVA), graphene oxide (GO), and PS nanobeads (40 nm) were prepared via an electrospinning process (Scheme 1a-①). The first heat treatment, that is, the process for the formation of bamboo-like N-CNTs, produced highly integrated N-CNTs containing Co nanometals inside each node (Scheme 1a-②). During this stage, the heat treatment of the precursor nanofibers with DCDA at 400 °C in a N_2 atmosphere initially produced metallic-Co nanoparticles, in which C formed by the decomposition of PVA restricted the grain growth and aggregation of the metallic Co nanocatalysts by surrounding them. Concurrently, PS nanobeads distributed in the GO matrix were decomposed into gas to uniformly form mesopores between the GO sheets. Additionally, the GO matrix was reduced to rGO under the reducing atmosphere during the initial step of the first heat treatment (Scheme 1a-②). The uniformly formed mesopores allowed the reducing gas to penetrate deep into the structure, forming uniform-sized Co nanometals. After the temperature of the reactor was increased to 800 °C, N-CNTs were grown similar to bamboo over the inner and outer parts of the rGO matrixed nanofibers and in the mesopores by using the metallic Co nanocrystals as catalysts with the CH_x and NH_3 gases generated from DCDA via catalytic chemical vapor deposition. DCDA is inexpensive, nonflammable, and solid at room temperature; thus, it has potential as an alternative precursor for N-doped C.[25] Interestingly, Co nanocrystals were located at each node of the bamboo-like N-CNTs because the CNTs grew as the Co nanoparticles moved and as C and N atoms dissociated by the CH_x and NH_3 gases were adsorbed and dissolved on the surface of the Co nanoparticles and dispersed by the force arising from the growth of the CNTs (Scheme S1, Supporting Information). The second heat treatment was conducted at 300 °C for 30 min in an air atmosphere, as shown in Scheme 1a-③. In general, it is very difficult to perform the conversion of Co nanocrystals surrounded by the CNT wall into $CoSe_2$ during selenization, because the H_2Se gas for selenization cannot penetrate the thick C layer of the CNT wall, as shown in Scheme 1b-①. To solve this, part of the CNT wall surrounding the Co metal was thermally etched during the second heat treatment (Scheme 1a-③), which allowed the penetration of H_2Se gas for the selenization of Co inside the wall, as shown in Scheme 1b-②. In the etching step, the Co metal was partially oxidized into Co_3O_4 during the heat treatment, which was inconsequential (Scheme 1-③). Finally, the third heat treatment for selenization was performed at 350 °C (Scheme 1-④).

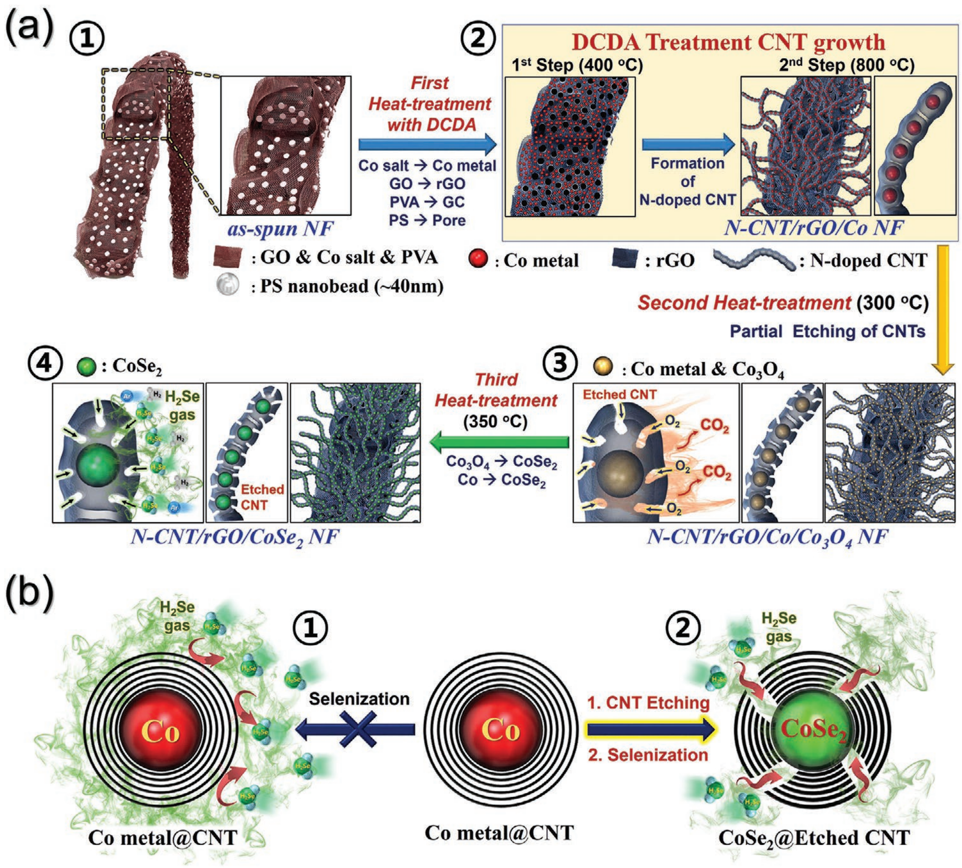

Scheme 1. a) Formation mechanism of the golden bristlegrass-like graphene matrixed nanofibers entangled with bamboo-like N-CNTs containing $CoSe_2$ nanocrystals at each node and b) efficient conversion of Co to $CoSe_2$ by partial etching strategy of N-CNT wall.

During the selenization process, the Co and Co_3O_4 nanoparticles inside the N-CNTs were successfully selenized into $CoSe_2$ via the reaction of these particles with the H_2Se gas that penetrated into the CNT walls in the reactor. Owing to the foregoing etching treatment for introducing defects into the CNT wall, the gas-diffusion process and phase conversion of Co and Co_3O_4 into $CoSe_2$ were easily achieved. Thus, the golden bristlegrass-like nanostructure comprising graphene matrixed nanofibers entangled with bamboo-like N-CNTs containing $CoSe_2$ nanocrystals at each node was successfully obtained via the series of heat treatments (Scheme 1-④).

To elucidate the formation mechanism of the N-CNT/rGO/$CoSe_2$ NF, the morphological and phase changes induced by each heat treatment of the composite nanofibers were investigated. The as-spun fibers stabilized at 150 °C in an air atmosphere exhibited a smooth surface and a uniform diameter of 600 nm, as shown in **Figure 1**a. It was difficult to confirm the aggregation of exposed GO sheets and the non-uniform thickness portion, indicating that both the GO and PS nanobeads were uniformly distributed in the composite after the electrospinning process. The presence of GO in the composite was confirmed by Raman analysis, as shown in Figure 1b. Typically, the Raman spectrum of GO exhibits a broad D-band peak at ≈1360 cm^{-1} and a G-band peak at 1600 cm^{-1}.[26,27] For the as-spun nanofibers, both the D and G bands were clearly observed, confirming the presence of GO. An additional peak near 2900 cm^{-1} was due to PVA, which was used as a precursor.[26] The broad band at 2700 cm^{-1} is known as the 2D band and confirms the presence of GO with few layers.[27] Additionally, according to the thermogravimetric (TG) analysis of the precursor composite fiber in Figure 1c, one-step weight loss occurred at ≈280 °C, at which the decomposition of the following precursors occurred: Co salt, GO sheets, PVA, and PS nanobeads. The X-ray diffraction (XRD) results indicated an amorphous C phase indexed at 25°, as shown in Figure 1d.

The bamboo-like N-CNTs were generated in the composite during the first heat treatment at 400 and 800 °C consecutively, as shown in **Figure 2**. After this heat treatment, the 1D nanofiber structure was retained, as shown in the field-emission scanning electron microscopy (FE-SEM) and transmission electron microscopy (TEM) images of Figure 2a,b. During the heat treatment of the precursor Co salt/GO/PVA/PS composite nanofibers with DCDA, the decomposition of PS nanobeads initially resulted in the formation of numerous mesopores with a mean diameter of 50 nm uniformly distributed in the composite as an intermediate step, as shown in Figure S1b,c, Supporting Information. These mesopores allowed for the efficient penetration of gases into the structure. Therefore, N-CNTs were grown in the composite via the reaction of the Co catalyst with CH_x and NH_3 gases generated by DCDA, as shown in Figure 2a–d. N has been regarded as a promising dopant of C, which can improve the electrical

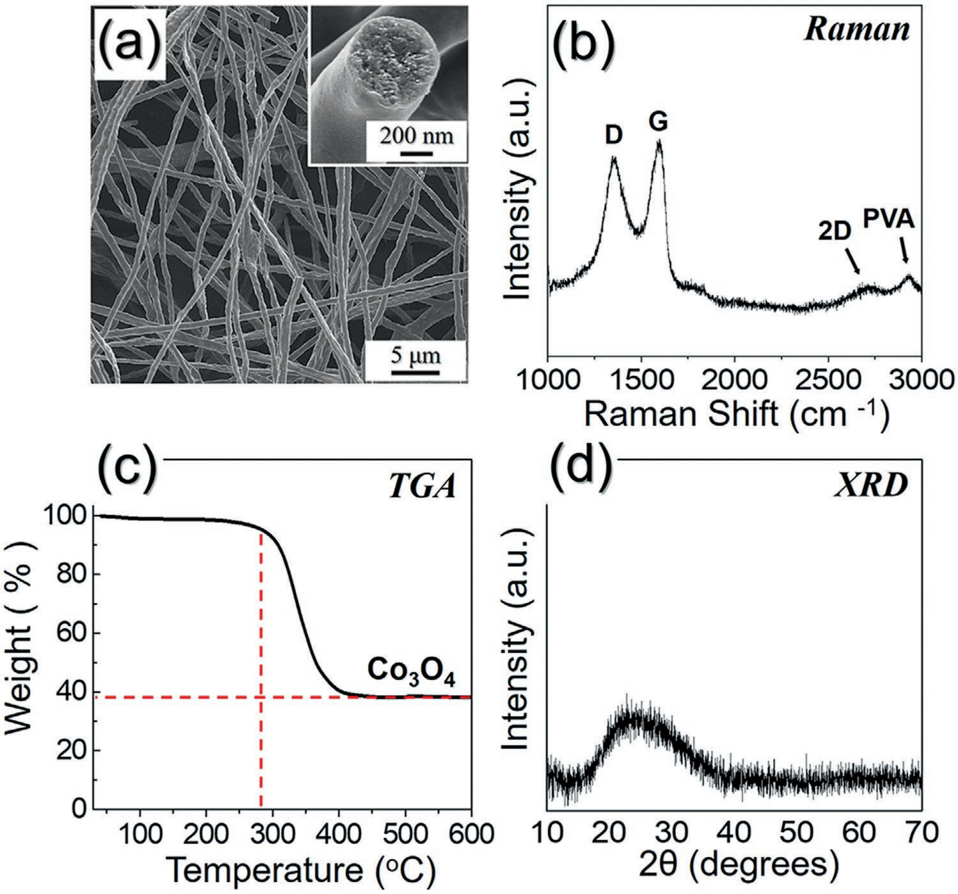

Figure 1. a) FE-SEM images, b) Raman spectrum, c) TG curve, and d) XRD pattern of the as-spun nanofibers obtained after stabilization at 150 °C.

conductivity of the cell owing to its smaller atomic radius and higher electronegativity compared with C.[28] Notably, the mesopores not only allowed the efficient penetration of reducing gases into the structure but also yielded a uniform distribution of nanosized Co metal in the composite. Additionally, the mesopores provided space for the growth of interconnected N-CNTs, which were bridged between GO sheets. The GO matrix was reduced under the reducing atmosphere. Therefore, the N-CNTs were expected to bridge the vertical defects for electron transfer in the rGO layers and increase the distance between the rGO sheets. The resulting N-CNTs exhibited a bamboo-like structure with an outer diameter of ≈20–30 nm and a length of up to several hundred nanometers, as shown in the high-resolution TEM image in Figure 2d. Additionally, metallic Co nanoparticles with lattice fringes separated by 0.20 nm corresponding to the (111) crystal plane (inset of Figure 2d) were located inside the CNT walls. Additionally, a graphitic carbon (GC) layer with lattice fringes separated by 0.34 nm corresponding to the (002) crystal plane of GC was formed around the Co metal, as shown in the inset of Figure 2d. The selected-area electron diffraction (SAED) pattern in Figure 2e shows rings of Co metal and carbonaceous materials (CNT, rGO, and GC) in the composite. The XRD pattern (Figure 2f) exhibits the characteristic peaks for Co metal and GC materials indexed at 26°.[29] The elemental-mapping images shown in Figure 2g revealed the presence of uniformly distributed Co, C, and N of the composite nanofibers.

In general, the thickness of the CNT walls was difficult to control. If CNT walls were thick, selenization of Co inside the CNTs could not occur, because the H_2Se gas could not penetrate the walls as indicated in Scheme 1b -①. Therefore, the second heat treatment for partially etching the CNT walls to allow the penetration of H_2Se gas was conducted at 300 °C for 30 min in air. The optimum etching temperature was determined by TG data of the composite obtained after first heat treatment (Figure S2, Supporting Information), in which the composite began to lose weight at ≈300 °C owing to CNT decomposition. Therefore, after the etching process at 300 °C, the unique rGO matrixed nanofibers entangled with bamboo-like N-CNTs were well maintained, as shown in **Figure 3**a,b. However, after the etching, the bamboo-like N-CNTs were more porous owing to the partial decomposition of the CNT walls, as shown in Figure 3b–d. Therefore, the penetration of H_2Se_2 gas inside the CNT walls for selenization could be allowed during the following selenization heat treatment as indicated in Scheme 1b -②. The Raman spectra of the nanofibers before and after etching process shown in Figure S3, Supporting Information also prove the formation of defect in CNTs after etching process. The D′ band at 1620 cm^{-1} suggesting high defect densities in CNTs was confirmed in Figure S3b, Supporting

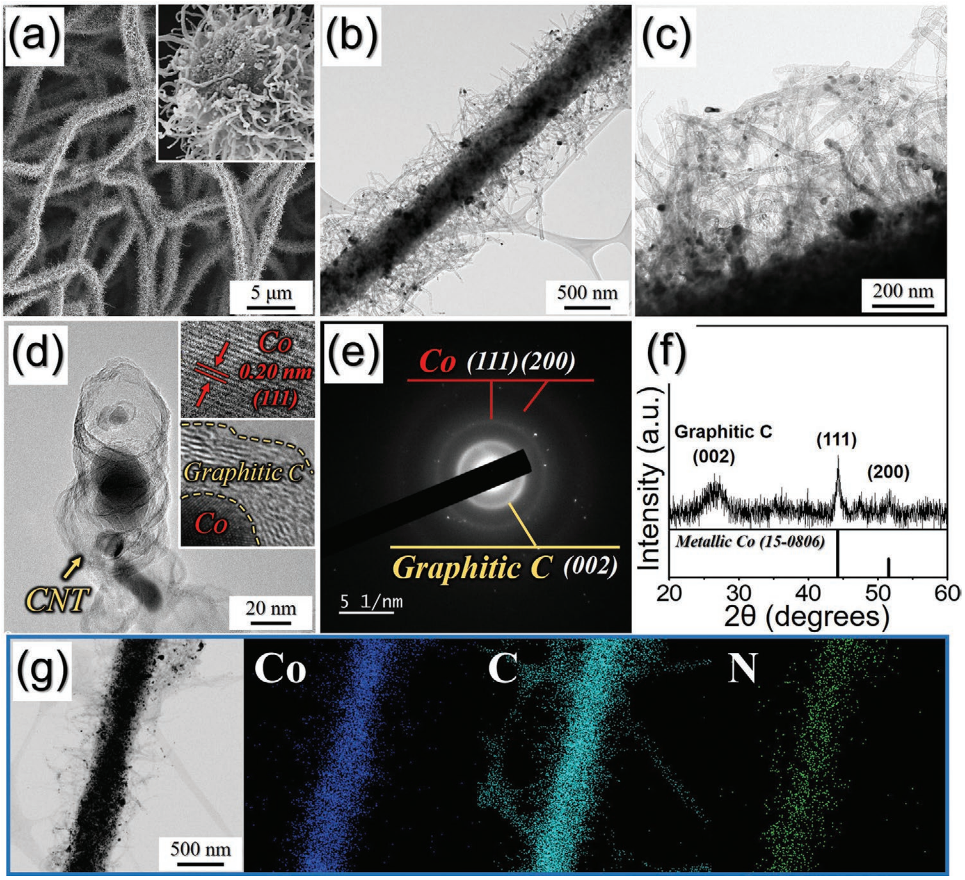

Figure 2. Morphologies, SAED, XRD patterns, and elemental mapping images of the composite nanofibers obtained after first heat-treatment of as-spun fibers at 400 °C and then 800 °C under N_2 atmosphere: a) FE-SEM images, b–d) HR-TEM images, e) SAED pattern, f) XRD pattern, and g) elemental mapping images.

Information. Concurrently, the partial oxidation of Co metal inside the CNT walls into Co_3O_4 nanoparticles occurred; therefore, lattice fringes separated by 0.24 nm corresponding to the (311) crystal plane of Co_3O_4 along with Co metal are observed in the inset images of Figure 3c. The SAED and XRD patterns of the composite confirmed the partial conversion into the Co_3O_4 phase and the presence of carbonaceous materials (Figure 3e,f). During the simple heat treatment performed at 300 °C in air, the amorphous C material in the composite was also selectively removed, which is confirmed by TG (Figure S4, Supporting Information) and elemental analysis (EA) in Table S1, Supporting Information, the total carbon contents decreased from 51 to 35 wt% after etching process. As shown in the elemental-mapping images of Figure 3g, the metallic Co, Co_3O_4 nanoparticles, rGO, and N-CNTs were distributed homogeneously in the composite nanofibers.

The golden bristlegrass-like graphene nanofibers entangled with bamboo-like N-CNTs containing $CoSe_2$ nanocrystals were finally obtained after the third heat treatment for selenization, as shown in **Figure 4**. The overall golden bristlegrass-like structure was well-maintained throughout, even after multi-step heat treatment, as shown in Figure 4a–d. The bamboo-like N-CNTs contained nanoparticles with a diameter of 5–10 nm at each node, as shown in Figure 4d. The successful phase conversion of Co and Co_3O_4 into $CoSe_2$ during selenization was confirmed by the HR-TEM lattice image in Figure 4e and the XRD pattern in Figure 4f. In the HR-TEM image (Figure 4e), ultrafine orthorhombic $CoSe_2$ nanoparticles with lattice fringes of 0.26 nm corresponding to the (111) crystal plane were observed inside the CNT wall.[30] The XRD pattern in Figure 4f confirms the presence of the $CoSe_2$ phase without impurities, indicating the complete selenization of metallic Co and Co_3O_4.[30,31] The mean crystallite size of $CoSe_2$ in N-CNT/rGO/$CoSe_2$ NF was calculated as 16 nm from the (111) peak width of the XRD pattern, which is determined from Scherrer's formula. In this study, the CNT walls were thick, which made the selenization of the Co particles surrounded by the CNT walls difficult. Therefore, the selenization of Co could not occur efficiently in the composite nanofibers subjected to heat treatment without the etching process, as confirmed in Figure S5, Supporting Information. The majority of the metallic Co phase remained still in the composite, along with $CoSe_2$, according to the XRD results in Figure S5c, Supporting Information. Based on the result, CNT defects were formed by the simple etching process, which allowed the phase conversion of Co and Co_3O_4 into $CoSe_2$ through the efficient penetration of H_2Se gas inside the CNT walls through the etched part. As shown in Figure 4g, the elemental-mapping images revealed that the ultrafine $CoSe_2$ nanocrystals were uniformly distributed

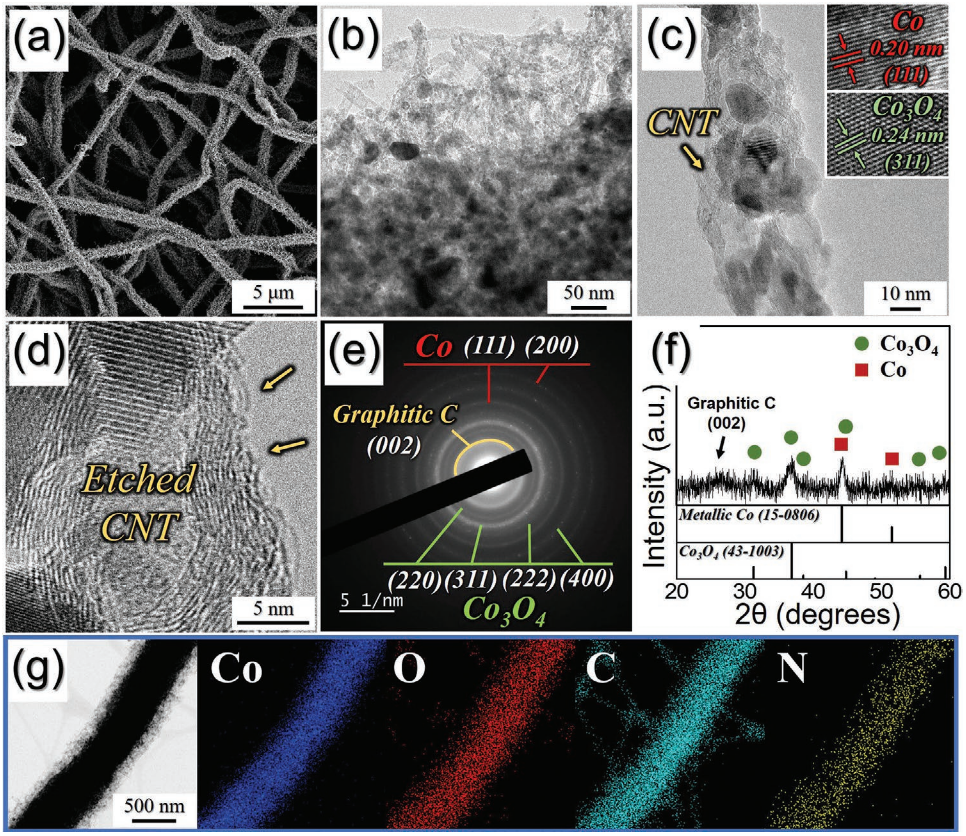

Figure 3. Morphologies, SAED, XRD patterns, and elemental mapping images of the composite nanofibers obtained after second heat-treatment at 300 °C for partial N-CNTs etching: a) FE-SEM image, b–d) HR-TEM images, e) SAED pattern, f) XRD pattern, and g) elemental mapping images.

over the golden bristlegrass-like graphene nanofibers entangled with bamboo-like N-CNTs.

The chemical nature of the N-CNT/rGO/$CoSe_2$ NF was analyzed via X-ray photoelectron spectroscopy (XPS), as shown in **Figure 5**. The survey spectrum of the N-CNT/rGO/$CoSe_2$ NF revealed the presence of Co, Se, N, and C (Figure 5a).[30,31] The high-resolution Co 2p XPS spectrum (Figure 5b) exhibited peaks at binding energies of 780.4 eV (Co $2p_{3/2}$) and 796.5 eV (Co $2p_{1/2}$), which were the Co^{2+} peaks of $CoSe_2$.[30,31] The additional Co^{3+} peaks at 778.6 eV for Co $2p_{3/2}$ and 793.6 eV for Co $2p_{1/2}$ were due to the partial surface oxidation of the sample in air.[30] Additionally, the two shake-up satellite peaks for the higher-energy Co 2p signal correspond to the antibonding orbital between Se and Co atoms.[30] In the high-resolution XPS spectrum of Se 3d (Figure 5c), the two peaks for Se $3d_{5/2}$ (54.8 eV) and for Se $3d_{3/2}$ (55.5 eV) are located at binding energies consistent with the metal-Se interactions of $CoSe_2$.[32,33] The peaks in the range of 58–61 eV are attributed to Co 3p and Se—O bonding at the surface of the composites.[30] The additional peak at 60.9 eV is attributed to Se—O bonding formed by the oxidation of metalloid Se under atmospheric conditions.[30] The high-resolution C 1s XPS spectrum (Figure 5d) exhibited several peaks corresponding to sp^2 C=O, C—O, C—N, and C—C bonds at 288.5, 286.4, 285.1, and 284.8 eV, respectively.[30,34] The C—N bond at 285.1 eV confirms the N-CNTs during the heat treatment.[30] The high-resolution N 1s spectrum shown in Figure 5e revealed the presence of three types of N species: pyridinic N at 398.7 eV, pyrrolic N at 400.4 eV, and graphitic N at 403.7 eV.[35] The atomic content of the N dopant was ≈3% of the N-CNT/rGO/$CoSe_2$ NF according to the EA results (Table S1, Supporting Information). According to previous reports, the vacancies and defect sites induced by N doping of C facilitate the insertion of more Na^+ ions as the number of cycles increases, resulting in excellent cycling stability.[36,37] The TG curve of the N-CNT/rGO/$CoSe_2$ NF is shown in Figure 5f. It indicates weight loss starting at 315 °C due to the conversion of $CoSe_2$ into $CoSeO_4$ and SeO_2, as well as the following conversion of $CoSeO_4$ into Co_3O_4 and the combustion of carbonaceous materials such as N-CNTs and rGO.[38] The content of the C materials in the N-CNT/rGO/$CoSe_2$ NF was estimated to be 14 wt% using the TG and EA results (Table S1, Supporting Information). Therefore, the amount of $CoSe_2$ phase in N-CNT/rGO/$CoSe_2$ NF is calculated as 83 wt%. Raman spectroscopy is sensitive to a material's electronic structures and thus is a useful technique for characterizing the crystallinity of C materials.[39,40] The Raman spectrum of the N-CNT/rGO/$CoSe_2$ NF in Figure S6a, Supporting Information exhibits the relative intensity ratio (I_D/I_G) of the D band (1360 cm^{-1}) to the G band (1600 cm^{-1}), which is generally used as a measure of structural disorders in graphitic materials,[39,40] was ≈0.92. The N_2 adsorption and desorption isotherms of the composite are presented in Figure S6b, Supporting Information. The isotherms were type IV with H3 hysteresis loops, indicating the presence of mesopores in the structure.[41] The Brunauer–Emmett–Teller

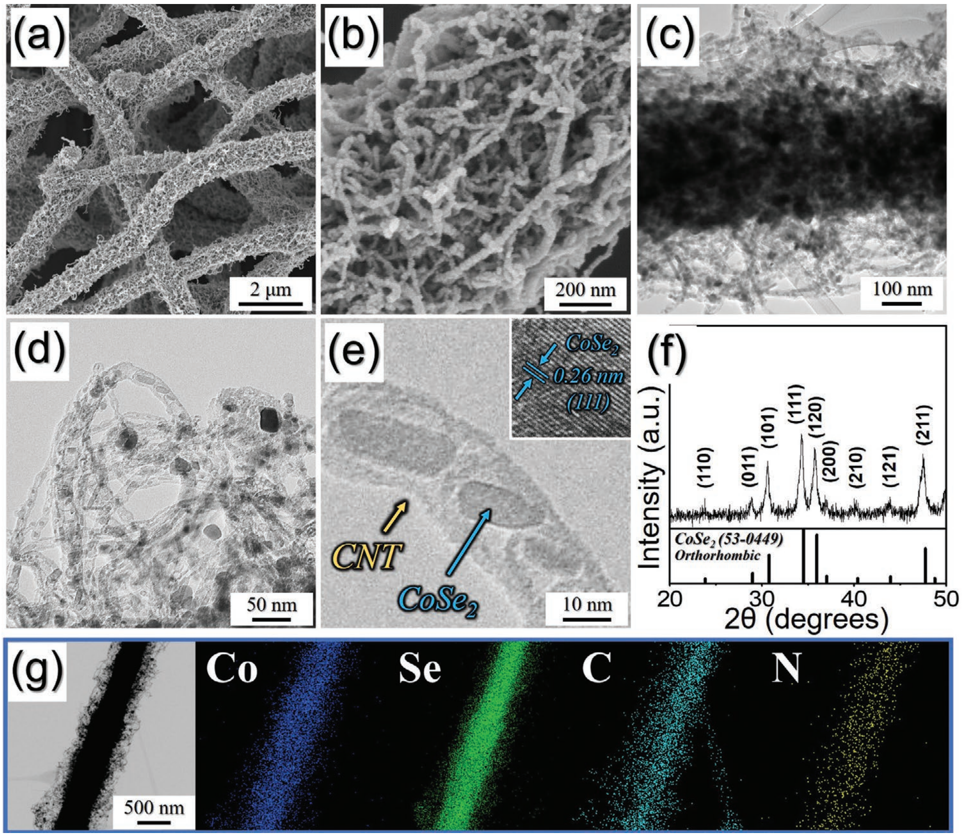

Figure 4. Morphologies, XRD pattern, and elemental mapping images of the golden bristlegrass-like graphene nanofibers entangled with bamboo-like N-CNTs containing $CoSe_2$ nanocrystals obtained after third heat-treatment at 350 °C for selenization: a,b) FE-SEM images, c–e) HR-TEM images, f) XRD pattern, and g) elemental mapping images.

(BET) surface area of the N-CNT/rGO/$CoSe_2$ NF was 22.8 m^2 g^{-1}. The pore-distribution curves shown in Figure S6c, Supporting Information indicate that the N-CNT/rGO/$CoSe_2$ NF had mesopores (<50 nm) and macropores (50–75 nm) owing to the 3D hierarchical nanostructure combined with N-CNTs vertically grown within the rGO sheet matrix. Additionally, the narrow peak of ≈4 nm was due to the tensile-strength effect of N_2 desorption.[42]

To prove the structural merits of the N-CNT/rGO/$CoSe_2$ NF for sodium-ion storage, bare $CoSe_2$-filled NF were also prepared, as shown in Figure S7c,d, Supporting Information. For this, bare intermediate Co_3O_4 nanofibers were prepared by directly heat-treating the as-spun nanofibers obtained from the spinning solution containing Co salt and PVA without GO and PS nanobeads at 600 °C in air, as shown in Figure S7a,b, Supporting Information. The selenization of the bare Co_3O_4 nanofibers at 500 °C produced bare $CoSe_2$-filled NF, as shown in Figure S7c,d, Supporting Information. In the case of the bare $CoSe_2$-filled NF, selenization was performed at a higher temperature of 500 °C to convert Co_3O_4 into $CoSe_2$ completely. The XRD patterns shown in Figure S7b,d, Supporting Information confirm the complete conversion of Co_3O_4 into $CoSe_2$ during the simple selenization process. The mean crystallite size of $CoSe_2$ in the bare $CoSe_2$-filled NF calculated from the half-width of the (111) peak using the Scherrer equation was 56 nm, which is higher than 16 nm of N-CNT/rGO/$CoSe_2$ NF.

The electrochemical properties of the N-CNT/rGO/$CoSe_2$ NF as an anode material for SIBs were compared with those of the bare $CoSe_2$-filled NF using carbonate-based electrolytes ($NaClO_4$ in ethylene carbonate/dimethyl carbonate [EC/DMC] with 5 wt% FEC), as shown in **Figure 6**. The cyclic voltammograms (CVs) of the samples for the first five cycles at a scan rate of 0.1 mV s^{-1} in the potential range of 0.001–3.0 V are shown in Figure 6a,b. For both samples, the cathodic peak at ≈0.78 V was assigned to the formation of metallic Co nanocrystals and Na_2Se due to the conversion reaction between the Na^+ and $CoSe_2$ during the first discharging process.[30,43,44] In the first charging process, two anodic peaks at 1.84 and 1.96 V were observed owing to the restoration of metallic Co and Na_2Se into $CoSe_2$ nanocrystals.[30,43,44] From the second cycle onward, two cathodic peaks were observed at 1.41 and 1.11 V, corresponding to the insertion of Na^+ into $CoSe_2$.[30,43,44] The peak shift to higher potential from the second cycle is due to the formation of ultrafine $CoSe_2$ nanocrystals after the first cycle.[6,29] The other cathodic peak at 0.7 V was assigned to the conversion reaction with further Na^+ insertion.[30,43,44] The discharge and charge curves of the samples for the first and second cycles at a current density of 0.5 A g^{-1} are shown in Figure 6c,d. In the initial discharge curve, the N-CNT/rGO/$CoSe_2$ NF exhibited sloped charge/discharge profiles and a comparatively short plateau at ≈0.89 V compared with the bare $CoSe_2$-filled NF owing to the ultrafine crystallite size of the $CoSe_2$. Typically, anode

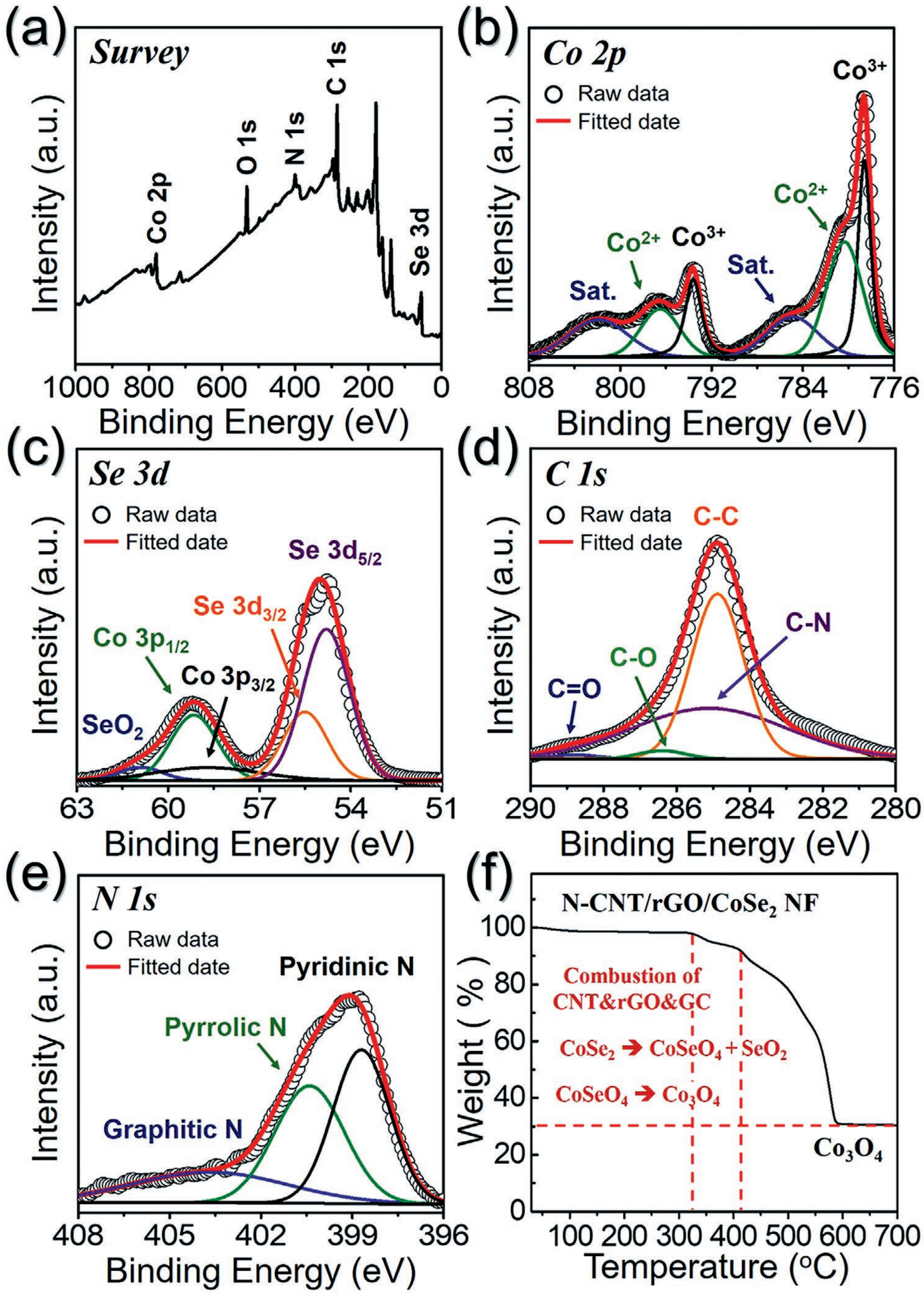

Figure 5. a) XPS survey spectrum, b) XPS Co 2p spectrum, c) XPS Se 3d spectrum, d) XPS C 1s spectrum, e) XPS N 1s spectrum, and f) TG curve of N-CNT/rGO/$CoSe_2$ NF.

materials with an amorphous phase or ultrafine nanocrystals exhibit sloped charge/discharge profiles, whereas crystalline materials exhibit flat plateaus.[45,46] Additionally, the bare $CoSe_2$-filled NF showed the plateau lower than that of N-CNT/rGO/$CoSe_2$ NF. The polarization is caused by slow Na^+-ion diffusion in the active material and increases in the resistance of the electrolyte in the bare $CoSe_2$-filled.[6,29] However, the unique nanostructure of N-CNT/rGO/$CoSe_2$ NF improved the Na^+-ion diffusion rate. Therefore, Na^+ insertion/desertion reactions could proceed more easily in the N-CNT/rGO/$CoSe_2$ NF. The initial discharge capacities of the N-CNT/rGO/$CoSe_2$ NF and the bare $CoSe_2$-filled NF were 645 and 531 mA h g^{-1}, respectively, and their corresponding Coulombic efficiencies were 72.4% and 83.5%, respectively. Although the amount of active material in the N-CNT/rGO/$CoSe_2$ NF was smaller than that of the bare sample in a unit, the N-CNT/rGO/$CoSe_2$ NF exhibited a larger discharge capacity than the bare sample. The polarization caused by slow Na^+-ion diffusion resulted in the low initial reversible specific capacity of the bare $CoSe_2$-filled NF. In general, polarization takes into account the resistance faced by

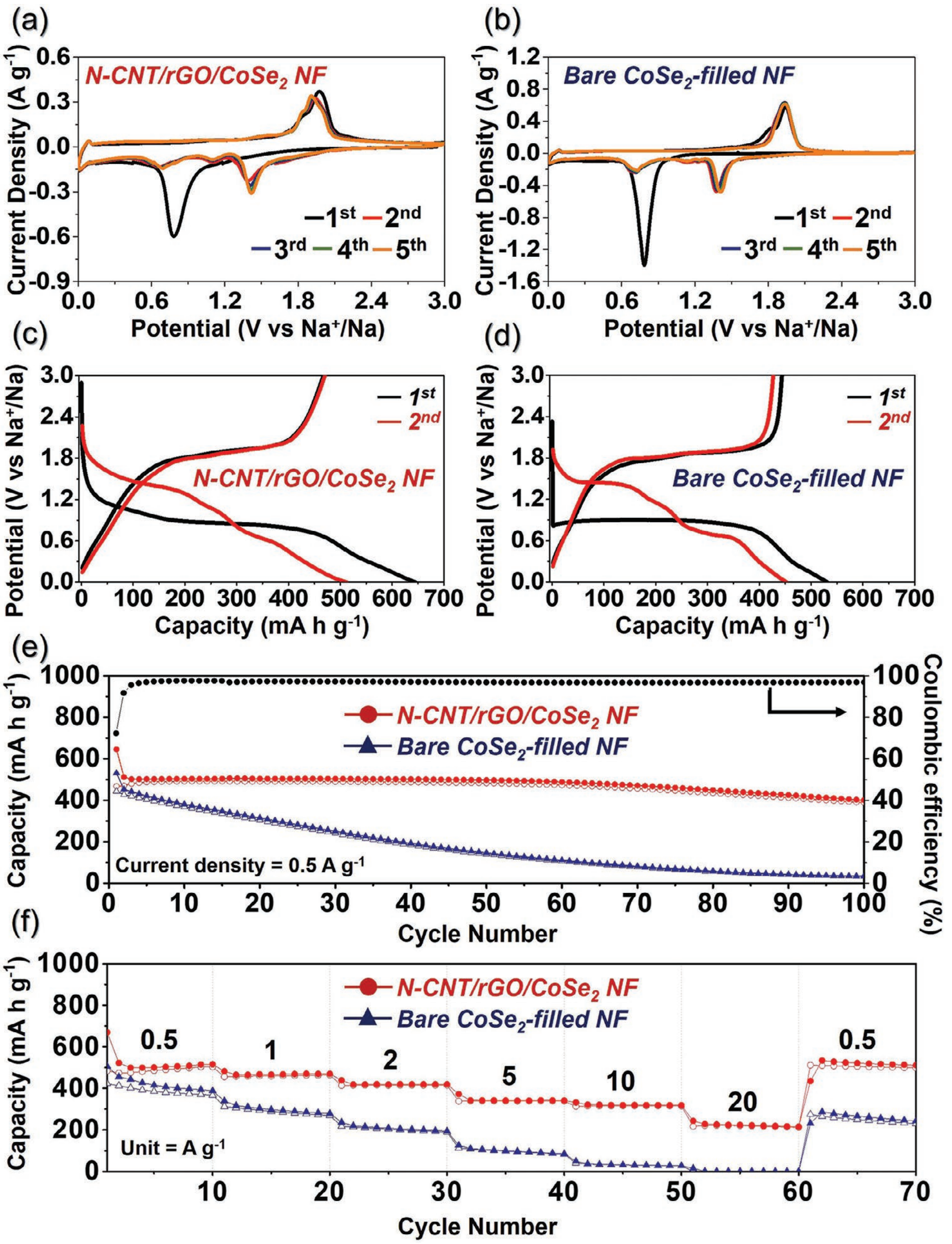

Figure 6. Electrochemical properties of N-CNT/rGO/CoSe$_2$ NF and bare CoSe$_2$-filled NF for sodium-ion storage of the cell assembled using carbonate-based electrolytes: a,b) cyclic voltammogram (CV) curves, c,d) discharge/charge curves at a current density of 0.5 A g^{-1}, e) cycle performances at a current density of 0.5 A g^{-1}, and f) rate properties.

the mass transfer (e.g., diffusion) process by which Na$^+$-ions are transported across the electrolyte from one electrode to another. Since, the polarization is current-dependent, it usually increases with increasing output current.[47,48] Therefore, the initial discharge/charge profile of the bare CoSe$_2$-filled NF at a sufficiently low current density of 0.05 A g^{-1} in Figure S8, Supporting Information indicated a discharge capacity of 879 mA h g^{-1} at the plateau at ≈1.05 V, which was higher than those analyzed at a current density of 0.5 A g^{-1}. It proved that the polarization of the N-CNT/rGO/CoSe$_2$ NF was efficiently overcome by designing and fabricating sophisticated electrode nanomaterials to provide a large surface area and short diffusion paths for ionic transport and electronic conduction, in this study. However, the relatively low initial Coulombic efficiency of the N-CNT/rGO/CoSe$_2$ NF was mainly due to the high initial irreversible capacity loss of C materials, such as N-CNT, rGO, and GC, for Na$^+$-ion storage.[49,50] However, the degree of irreversibility during the first cycle could be effectively reduced by pre-sodiation of the electrode material.[51,52]

The cycling performance of the nanofibers at a current density of 0.5 A g^{-1} with the carbonate-based electrolytes is shown in Figure 6e. The bare CoSe$_2$-filled NF exhibited extremely fast capacity fading during the cycles; the discharge capacity after the 100th cycle was only 34 mA h g^{-1}. This is owing to the structural destruction, the large volume change of $CoSe_2$ during repeated Na^+ ion insertion and extractions was not accommodated during the cycling. In contrast, the N-CNT/rGO/$CoSe_2$ NF exhibited good cycle stability for up to 100th cycles. The discharge capacities of the N-CNT/rGO/$CoSe_2$ NF at the second and 100th cycles were 512 and 400 mA h g^{-1}, respectively. The rGO sheets, vertically interconnected N-CNTs surrounding $CoSe_2$ nanoparticles, and void space between the elements effectively buffered the volume expansion of $CoSe_2$ nanoparticles during the cycling. Additionally, the aggregation of the $CoSe_2$ nanoparticles was restrained, maintaining the structural stability. In order to calculate the capacity contribution of both N-CNT and rGO matrix to the N-CNT/rGO/$CoSe_2$ NF electrode, N-CNT/rGO/$CoSe_2$ NF was etched with HCl solution, thus pure N-CNT/rGO framework was obtained in Figure S9, Supporting Information. Complete removal of $CoSe_2$ from the structure was proven by EDS as shown in Figure S9a, Supporting Information. The first discharge–charge profile confirmed that the N-CNT/rGO framework was pure carbon with discharge and charge capacities of 595 and 187 mA h g^{-1}, respectively, as shown in Figure S9b, Supporting Information. The pure N-CNT/rGO framework exhibited a reversible discharge capacity of 140 mA h g^{-1} at a current density of 0.5 A g^{-1} for the 100th cycle as shown in Figure S9c, Supporting Information. Therefore, the contribution of the N-CNT/rGO framework to the discharge capacity of N-CNT/rGO/$CoSe_2$ NF electrode could be estimated to be 35%. The rate properties of both samples at current densities from 0.5 to 20.0 A g^{-1} were shown in Figure 6f. The N-CNT/rGO/$CoSe_2$ NF showed excellent rate performance even at high current densities. The N-CNT/rGO/$CoSe_2$ NF had final discharge capacities of 516, 470, 420, 341, 318, and 215 mA h g^{-1} at current densities of 0.5, 1, 2, 5, 10, and 20 A g^{-1}, respectively. Additionally, the discharge capacity recovered well to 512 mA h g^{-1} when the current density was reduced to 0.5 A g^{-1}. In contrast, the discharge capacity of the bare $CoSe_2$-filled NF decreased from 388 mA h g^{-1} to almost zero as the current density increased from 0.5 to 20.0 A g^{-1}.

The Na-ion storage performance of the nanofibers was also investigated in voltage range of 0.3–2.9 V to remove the effect of side reactions, using ether-based electrolytes ($NaCF_3SO_3$ in diethylene glycol dimethyl ether [DEGDME]), and the results are shown in **Figure 7**. It has been reported that, in general, ether-based electrolytes have a low activation-energy barrier for Na^+-ion diffusion on the structure and high stability during repeated cycles, which contribute to the good electrochemical properties of the cells for SIBs with metal selenide anodes.[53,54] The CVs of the N-CNT/rGO/$CoSe_2$ NF and bare $CoSe_2$-filled NF for the first five cycles at a scan rate of 0.1 mV s^{-1} are shown in Figure S10, Supporting Information. In the first cycle, both samples exhibited a sharp peak at 1.01 V in the cathodic scan, which is correlated with the activation process of $CoSe_2$ and the possible formation of solid-electrolyte interphase (SEI) layers.[31,55] The discharge/charge profiles of the N-CNT/rGO/$CoSe_2$ NF at a current density of 1.0 A g^{-1} are shown in Figure 7a. According to the discharge/charge profiles and the CV curve (Figure 7a and Figure S10, Supporting Information) for the N-CNT/rGO/$CoSe_2$ NF, the $CoSe_2$ phase experienced an activation–stabilization process during the discharge/charge cycles.[31,55] After the activation–stabilization process, three reduction peaks at 1.6, 1.1, and 0.7 V, as well as two oxidation peaks at 1.5 and 1.8 V, were consistently observed in the subsequent cycle.[55,56] The first reduction peak at 1.6 V corresponds to Na^+-ion intercalation, whereas the two reduction peaks at 1.1 and 0.7 V correspond to two conversion reactions that formed $CoSe/Na_2Se$ and Co/Na_2Se, respectively.[55,56] The two oxidation peaks correspond to the formation of Na_xCoSe_2 and the fully charged product $CoSe_2$, respectively.[55,56] In order to confirm the conversion reaction between the electrode and Na^+-ion, ex situ XRD and SAED measurements for the N-CNT/rGO/$CoSe_2$ NF at different discharge/charge states were performed in Figure S11, Supporting Information. At discharged 0.8 V, the peak of CoSe and $NaSe_2$ phases are detected. At fully discharged 0.01 V, the peaks of $NaSe_2$ also appear, and a peak of Co is observed from the XRD pattern and SAED crystal planes. At fully charged state (3.0 V), there is no obvious characteristic signal in the XRD pattern, but the SAED pattern displays the planes of $CoSe_2$. These observations are consistent with the results of previously reported works,[57] indicating a series of conversion reactions. Therefore, the discharge and charge processes are summarized below.

Sodiation:

$$CoSe_2 + xNa^+ + xe^- \rightarrow Na_xCoSe_2 \tag{1}$$

$$Na_xCoSe_2 + xNa^+ + xe^- \rightarrow CoSe + Na_2Se \tag{2}$$

$$CoSe + 2Na^+ + 2e^- \rightarrow Co + Na_2Se \tag{3}$$

Desodiation:

$$Co + 2Na_2Se \rightarrow Na_xCoSe_2 + (4-x)\,Na^+ + (4-x)\,e^- \tag{4}$$

$$Na_xCoSe_2 \rightarrow CoSe_2 + xNa^+ + xe^- \tag{5}$$

The cycling performance of the N-CNT/rGO/$CoSe_2$ NF and bare $CoSe_2$-filled NF, which was evaluated using the ether-based electrolytes at a current density of 1.0 A g^{-1}, are shown in Figure 7b. The initial discharge capacities of the N-CNT/rGO/$CoSe_2$ NF and bare $CoSe_2$-filled NF were 448 and 402 mA h g^{-1}, respectively, and their corresponding Coulombic efficiencies were 88% and 79%, respectively. The high Coulombic efficiency of the N-CNT/rGO/$CoSe_2$ NF is because the electrolyte decomposition could be suppressed by using the ether-based electrolytes, resulting in the formation of a negligible SEI film on the sample, enabling Na^+ solvent transport to the electrode.[58,59] On the other hand, carbonate-based electrolytes have been reported to form relatively thick insulating SEI layers on the sample surface, which block Na^+ solvent transport.[58,59] To confirm that, the Coulombic efficiencies of the pure N-CNT/rGO framework obtained by etching the N-CNT/rGO/$CoSe_2$ NF with HCl was investigated using each electrolyte (Figure S12, Supporting Information). The pure N-CNT/rGO framework using ether-based electrolytes showed better Coulombic efficiencies compared to those of carbonate-based electrolytes regardless of potential windows, as shown in Figure S12, Supporting Information. Additionally, the N-CNT/rGO/$CoSe_2$ NF exhibited stable cycle property at a current density of 1.0 A g^{-1}

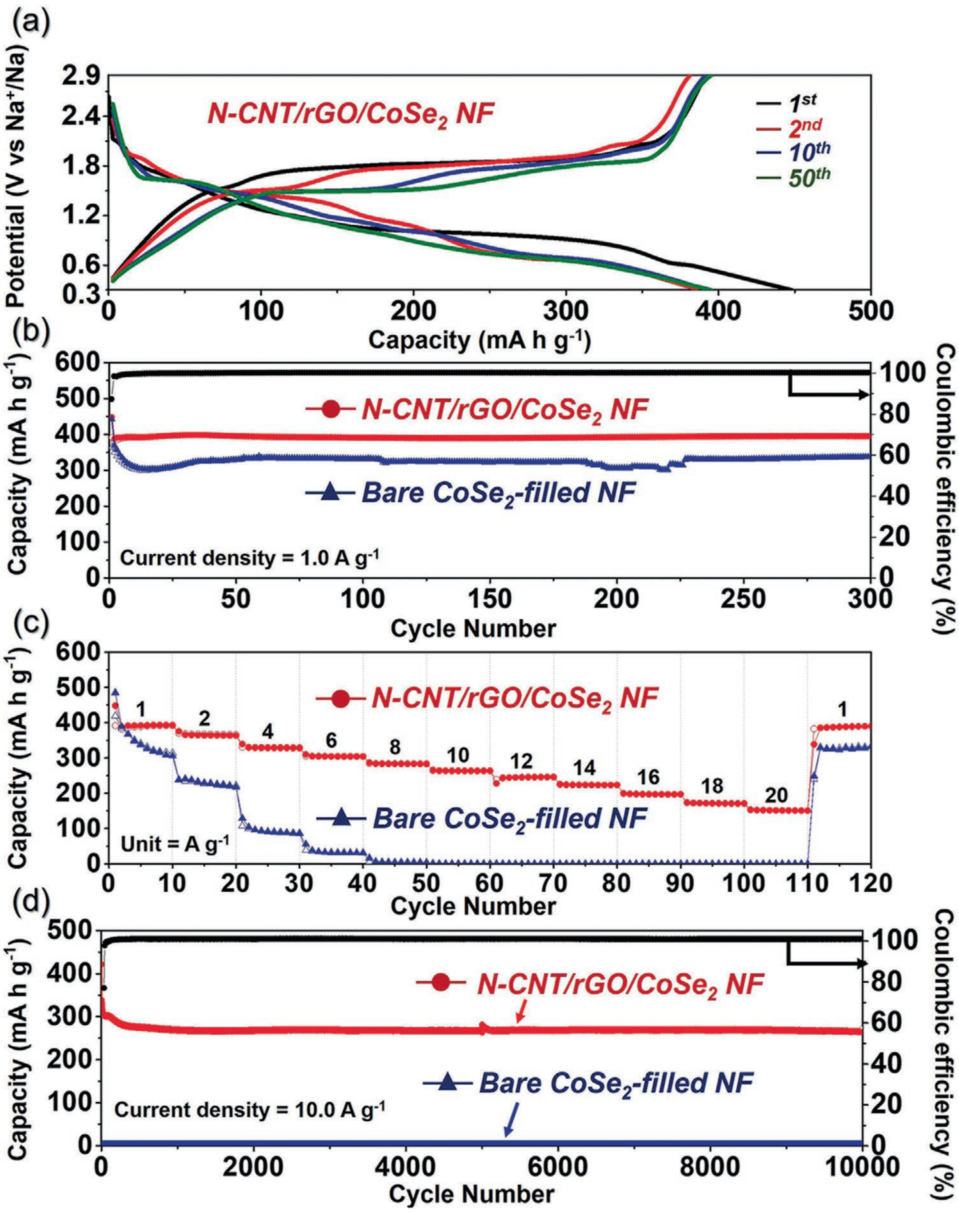

Figure 7. Electrochemical properties of N-CNT/rGO/CoSe$_2$ NF and bare CoSe$_2$-filled NF for sodium-ion storage of the cell assembled using ether-based electrolytes: a) discharge/charge curves of N-CNT/rGO/CoSe$_2$ NF at the current density of 1.0 A g^{-1}, b) cycle properties, c) rate properties, and d) long-term cycle properties at a current density of 10.0 A g^{-1}.

during 300th cycles, as shown in Figure 7b. In the case of the bare CoSe$_2$-filled NF, the discharge capacity initially decreased with increasing cycles, reaching 303 mA h g^{-1} at the 15th cycle and subsequently showed good cycle stability during cycles while they had fast capacity degradation when using carbonate-electrolytes (Figure 6e). The electrochemical properties were affected by the electrolytes in two aspects, including the solvent–salt stability and the reaction energy barrier. Carbonate-based electrolytes, as reported, would react with anionic group, leading to capacity decay.[53] However, no such problem occurs in the ether-based electrolyte, thus guaranteeing good cyclability. In addition, solvent–salt interactions decide the steric hindrance by the coordination environment (carbonate or ether group coordinates to Na$^+$ ions.[60] The Na-carbonate group suffers from ponderous volume, exhibiting inevitable obstruction and sluggish kinetics during the electrochemical reaction.[53] On the contrary, the ether-based electrolytes possess a 1D flexible chain morphology. Swift intercalation with smaller reaction energy barrier would enhance the reaction kinetics between Na-DGM and the active electrode material.

The excellent rate performance of the N-CNT/rGO/CoSe$_2$ NF was compared with that of the bare CoSe$_2$-filled NF, as shown in Figure 7c. The N-CNT/rGO/CoSe$_2$ NF had final discharge capacities of 395, 363, 328, 304, 283, 263, 246, 223, 197, 171, and 151 mA h g^{-1} at current densities of 1, 2, 4, 6, 8, 10, 12, 14, 16, 18, and 20 A g^{-1}, respectively. Additionally, the discharge capacity

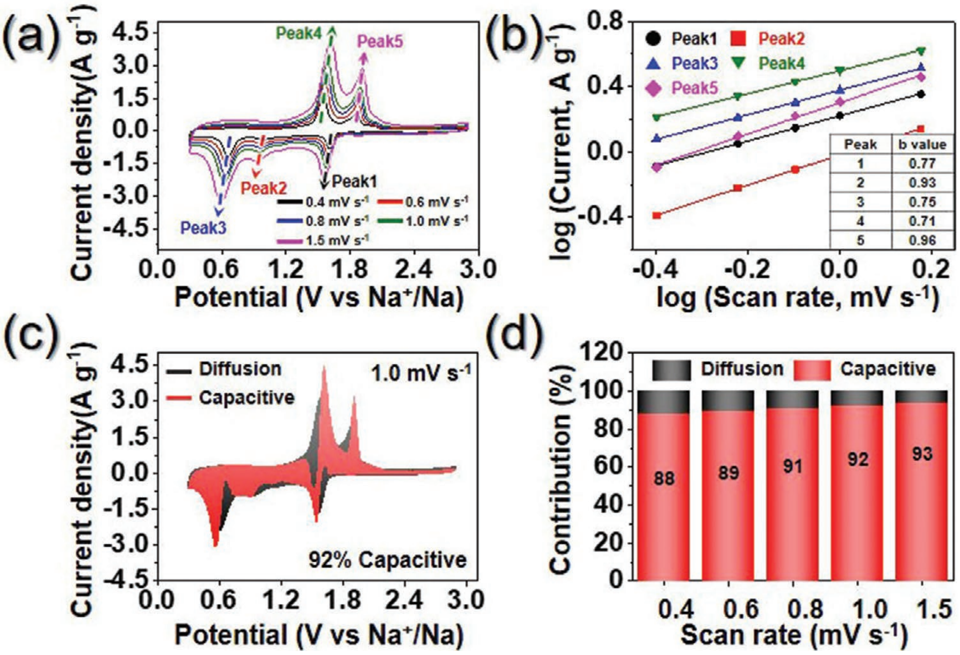

Figure 8. Electrochemical reaction dynamics analysis of N-CNT/rGO/CoSe$_2$ NF: a) CV curves obtained at various scan rates, b) current response (*i*) versus scan rate (*n*) at each redox peak, c) CV curve with the capacitive fraction shown by the red region at a scan rate of 1.0 mV s^{-1}, and d) bar chart showing the percentage of the capacitive contribution at different scan rates.

recovered well to 390 mA h g^{-1} when the current density was reduced to 1.0 A g^{-1}, even after operation at high current densities. In contrast, the discharge capacity of the bare CoSe$_2$-filled NF decreased from 304 to 31 mA h g^{-1} as the current density increased from 1.0 to 6.0 A g^{-1}. Subsequently, bare CoSe$_2$-filled NF does not show capacities due to the kinetics problems related to diffusion of Na$^+$ ions and transport of electrons during cycles at high current densities over 8 A g^{-1}. The excellent rate capability of the N-CNT/rGO/CoSe$_2$ NF at high current densities is attributed to the unique nanostructure, which had various advantages. First, the rGO sheets and N-CNTs of the matrix contributed to the high electrical conductivity of the electrode, which facilitated fast electron transfer by improving the electrical contact between the active sites of the CoSe$_2$ nanoparticles and the electrode. The porous structure of the N-CNT/rGO/CoSe$_2$ NF also allowed efficient penetration of the liquid electrolyte into the electrode during cycling, which promoted the electrochemical reaction during cycling. Additionally, efficient electron transport was possible in the vertical direction as well as the longitudinal direction, because the N-CNTs were interconnected and grown in the vertical direction between the rGO sheets, as shown in Scheme S2, Supporting Information. These factors could solve the kinetics problems related to diffusion of Na$^+$ ions and transport of electrons during repeated charge/discharge processes, thereby resulting in superior capacities compared to the bare CoSe$_2$-filled NF in the case of very high current densities.

The long-term cycling performances of the N-CNT/rGO/CoSe$_2$ NF and bare CoSe$_2$-filled NF at an extremely high current density of 10 A g^{-1} are shown in Figure 7d. In the case of N-CNT/rGO/CoSe$_2$ NF, the discharge capacities for the 100th and 10 000th cycles were 299 and 264 mA h g^{-1}, respectively, and the capacity retention measured from the 100th cycle was 89%. The N-CNT/rGO/CoSe$_2$ NF exhibited high Coulombic efficiencies of 99.99% from the 30th cycle onward, even at a high current density of 10 A g^{-1}. On the contrary, bare CoSe$_2$-filled NF does not show capacities due to the kinetics problems related to diffusion of Na$^+$ ions and transport of electrons during cycles at extremely high current density of 10 A g^{-1}.

To elucidate the excellent rate capability of the N-CNT/rGO/CoSe$_2$ NF in SIBs, the electrochemical kinetics of the cell assembled with ether-based electrolytes was investigated via cyclic voltammetry between 0.3 and 2.9 V at different scan rates (**Figure 8**a). In general, the capacitive contribution of the cell is characterized by analyzing the measured current (*i*) at various scan rates (*ν*), according to the following relationship.[54–56]

$$i = a\nu^{b} \tag{6}$$

$$\log(i) = b\log(\nu) + \log(a) \tag{7}$$

where *a* and *b* are adjustable parameters. If *b* is close to 1, the electrochemical reaction process is mainly controlled by the capacitive contribution.[54–56] When *b* approaches 0.5, this corresponds to ionic diffusion in the electrochemical reaction process.[54–56] Figure 8b presents log(*i*) versus log(*ν*) plots at three reduction peaks (peak 1, 2, and 3) and two oxidation peaks (peaks 4 and 5), and the *b*-values were calculated using the slope. The *b*-values for peaks 1, 2, 3, 4, and 5 of the N-CNT/rGO/CoSe$_2$ NF were 0.77, 0.93, 0.75, 0.71, and 0.96, respectively, which were close to 1.0, suggesting a dominant capacitive behavior in the redox process. To gain further insight into the capacity contribution, the total stored charge in the

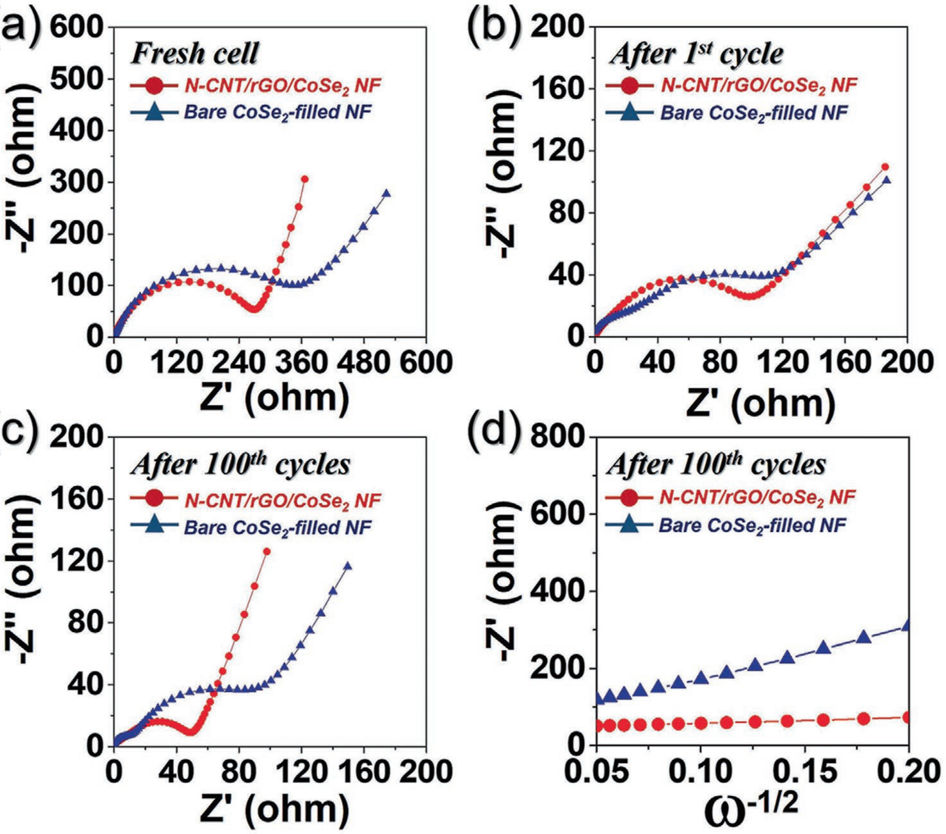

Figure 9. a–c) Nyquist impedance plots and d) relationships between the real part of the impedance (Z_{re}) and $\omega^{-1/2}$ of N-CNT/rGO/CoSe$_2$ NF and bare CoSe$_2$-filled NF: a) fresh cells, b) after the first cycle, and c,d) after the 100th cycles.

electrode material was separated into capacitive and diffusion-limited elements. The capacitive contribution can be quantitatively distinguished using the following equation:[54–56]

$$i = k_1\nu + k_2\nu^{1/2} \tag{8}$$

where $k_1\nu$ and $k_2\nu^{1/2}$ represent the capacitive contribution and ionic diffusion, respectively.[54–56] The constants k_1 and k_2 are determined by the slope and intercept, respectively, in the plot of $i(\mathrm{V})/\nu^{1/2}$ versus $\nu^{1/2}$ for each potential. The capacitive contribution of the N-CNT/rGO/CoSe$_2$ NF at the scan rate of 1.0 mV s^{-1} is shown in Figure 8c and occupied an area of 92%. Additionally, as shown in Figure 8d, the capacitive contribution of the N-CNT/rGO/CoSe$_2$ NF to the total capacity gradually increased as the scan rate increased from 0.4 to 1.5 mV s^{-1}.

The capacitive contribution at 1.5 mV s^{-1} increased to 93%, which agrees well with the high b close to 1 in Figure 8b. Even at the low scan rate of 0.4 mV s^{-1}, the N-CNT/rGO/CoSe$_2$ NF exhibited a large capacitive contribution of 88%. The bare CoSe$_2$-filled NF exhibited a much smaller capacitive contribution than the N-CNT/rGO/CoSe$_2$ NF, as shown in Figure S13, Supporting Information. Commonly, the capacitive behavior in battery electrodes is closely related to the electrochemical dynamics or kinetics. Thus, the high ratio of the capacitive-controlled contribution in the battery electrodes indicates relatively fast transport kinetics of Na$^+$ ions, which improved the rate capability of the electrodes. The rGO sheets and N-CNTs of the matrix facilitated fast electron transfer by improving the electrical contact between the active sites of the CoSe$_2$ nanoparticles and the electrode. Additionally, efficient electron transport was possible in the vertical direction because the N-CNTs were interconnected and grown in the vertical direction on the rGO sheet matrix.

To further study the electrochemical kinetics of the electrodes, the electrochemical impedance spectroscopy (EIS) spectra of the N-CNT/rGO/CoSe$_2$ NF and the bare CoSe$_2$-filled NF were measured using cells assembled with carbonate-based electrolytes before and after cycling, as shown in **Figure 9**. The Nyquist plots exhibit semicircles in the medium-frequency range, which indicate the charge-transfer resistance (R_{ct}) of the electrode.[54] The Nyquist plots of the samples were obtained via deconvolution using a Randle-type equivalent-circuit model (Figure S14, Supporting Information).[61] As shown in Figure 9a, the N-CNT/rGO/CoSe$_2$ NF had a lower R_{ct} (288 Ω) than the bare CoSe$_2$-filled NF (395 Ω) before cycling, owing to the fast interface kinetics of the N-CNT/rGO/CoSe$_2$ NF. As shown in Figure 9b, after the first cycle, the R_{ct} values of the N-CNT/rGO/CoSe$_2$ NF and the bare CoSe$_2$-filled NF were significantly reduced to 113 Ω and 126 Ω, respectively. This is because of the transformation of the CoSe$_2$ crystals into ultrafine nanocrystals during the initial cycling.[45] The low R_{ct} values of the N-CNT/rGO/CoSe$_2$ NF were well maintained (54 Ω) even after 100th cycles of repeated Na$^+$-ion insertion and desertion reactions, whereas the bare CoSe$_2$-filled NF exhibited an increased charge-transfer resistance (107 Ω), as shown in Figure 9c. The high electrical conductivity and structural stability of the N-CNT/rGO/CoSe$_2$ NF during the repeated Na$^+$-ion charge/discharge processes resulted in low R_{ct} values. The relationship between Z' (the real part of the impedance spectra) and $\omega^{-1/2}$ (where ω represents the angular frequency) in the low-frequency region after 100th cycles is shown in Figure 9d. The less steep slope at low frequencies indicates the higher Na$^+$-ion diffusivity of the electrodes. The slope of the curve for the N-CNT/rGO/CoSe$_2$ NF after the 100th cycle was significantly lower than that of the bare CoSe$_2$-filled NF, suggesting that the Na$^+$ ion diffusion rate was significantly higher for the N-CNT/rGO/CoSe$_2$ NF. This result agrees well with the superior rate performance of the N-CNT/rGO/CoSe$_2$ NF, as shown in Figure 7c. The high electrical conductivity, rGO, and N-CNTs promoted the electron-transfer kinetics, which led to an improved Na$^+$-ion diffusion rate. To confirm the structural integrity of the N-CNT/rGO/CoSe$_2$ NF after cycling, the electrodes of the cells assembled with carbonate-based electrolytes after 100th cycles were confirmed via FE-SEM. As shown in **Figure 10**a, the original fiber morphology of the N-CNT/rGO/CoSe$_2$ NF was well retained without structural destruction. The volume expansion of CoSe$_2$ was effectively accommodated during the repeated charge/discharge processes. However, the bare CoSe$_2$-filled NF failed to withstand the internal stress because of volume changes; it fragmented into several pieces and aggregated into bulk powder after cycling, as shown in Figure 10b. These results confirmed the high structural robustness of the N-CNT/rGO/CoSe$_2$ NF, which led to the superior cycle property of the cell in this study.

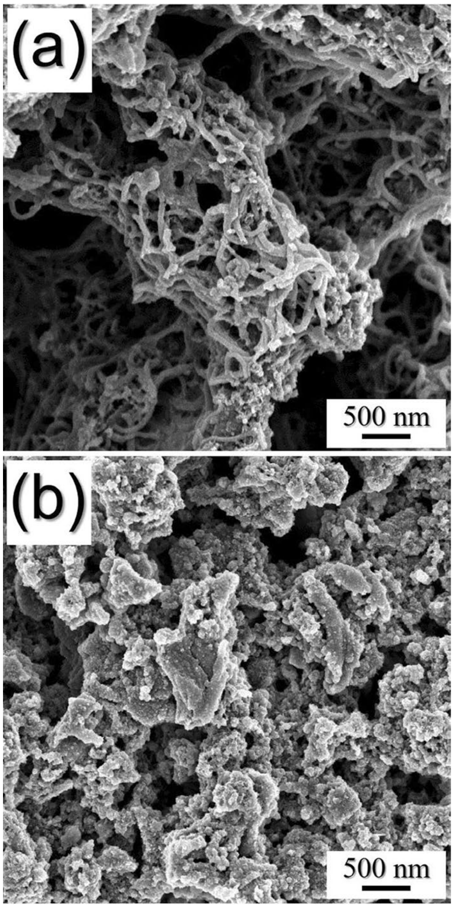

Figure 10. FE-SEM images of a) N-CNT/rGO/CoSe$_2$ NF and b) bare CoSe$_2$-filled NF obtained after the 100th cycles.

On the basis of the foregoing results, the outstanding Na-ion storage properties of the sophisticatedly designed N-CNT/rGO/CoSe$_2$ NF, such as the high specific capacity, good cycling stability, and excellent rate capability, were due to synergistic effects. The unique and porous nanostructure alleviated volume expansion during cycling and allowed efficient penetration of the liquid electrolyte into the electrode. Additionally, the rGO sheets and N-CNTs contributed to the high electrical conductivity of the electrode, which facilitated fast electron transfer by improving the electrical contact between the active sites of the CoSe$_2$ nanoparticles. Finally, the N-CNTs, which were interconnected and grown in the vertical direction between the rGO sheets, provided efficient electron transport in the vertical and longitudinal directions.

3. Conclusions

As high-performance anodes for sodium-ion batteries, golden bristlegrass-like graphene nanofibers entangled with N-CNTs containing CoSe$_2$ nanocrystals were designed and synthesized via electrospinning and multi-step heat treatment. Bamboo-like N-CNTs were generated both on the rGO matrixed nanofiber surface and as bridges between the rGO sheets and mesopores formed via the decomposition of PS nanobeads. The N-CNTs were chemically interconnected with the homogeneously distributed rGO sheets with the help of DCDA. By partially introducing defects into the CNT walls during heat treatment, the gas-diffusion process and phase conversion of Co into CoSe$_2$ were easily achieved. Consequently, the synthesized N-CNT/rGO/CoSe$_2$ NF exhibited high cycling and rate performance even at extremely high current densities. The synergistic effect of the golden bristlegrass-like unique structure and the N-CNTs/rGO composite resulted in efficient anode materials for SIBs. It is believed that the unique nanostructure comprising various metal compounds, N-CNT, and rGO synthesized via the proposed strategy is suitable for various applications, including energy storage.

4. Experimental Section

Sample Preparation: The golden bristlegrass-like graphene matrixed nanofibers entangled with bamboo-like N-CNTs containing CoSe$_2$ nanocrystals at each node (denoted as N-CNT/reduced graphene oxide (rGO)/CoSe$_2$ NF) were prepared through electrospinning and a subsequent multi-step heat-treatment process. For this, a colloidal solution for electrospinning was prepared by adding 0.5 g of graphene oxide (GO) and 2.0 g of PS nanobeads (≈40 nm) to a mixed solution containing 6.0 g of cobalt acetate tetrahydrate ($Co(CH_3COO)_2 \cdot 4H_2O$, DaeJung Chemicals & Metals Co., Ltd., 98%), 3.0 g of poly(vinyl alcohol) (PVA, Kanto Chemical Co., Inc., M_w: 2000), and 30 mL of ethyl alcohol (Duksan, 99.9%) with vigorous stirring overnight. The size-controlled PS nanobeads (40 nm) were synthesized using an emulsifier-free emulsion polymerization method, as described in a previous work study.[62] The GO was prepared from graphite flakes via the modified Hummers method.[63] The prepared spinning solution was loaded into a plastic syringe equipped with a 21-gauge stainless-steel needle. The solution was ejected at a flow rate of 4 mL h^{-1} onto a drum collector covered with Al foil. During the electrospinning process, the distance between the tip and the collector was fixed at 15 cm, and the rotation speed of the drum collector was set at 150 rpm. The applied voltage between the collector and the needle tip was 20 kV. The resulting as-spun $Co(CH_3COO)_2$-PVA-GO-PS nanobeads composite fibers were stabilized in an air atmosphere at 150 °C for 2 days. Subsequently, the initial heat-treatment step was conducted at 400 °C for 3 h and then at 800 °C for 1 h in a N_2 atmosphere to generate N-doped CNTs in the composite. During the initial step, as-spun $Co(CH_3COO)_2$-PVA-GO-PS composite fibers and DCDA (Sigma–Aldrich, 99%) powder (as the C and N source) were loaded into a covered alumina boat and placed in a quartz tube reactor. The second heat-treatment step was conducted at 300 °C for 30 min at a heating rate of 5 °C min^{-1} in an air atmosphere to perform partial etching of the CNTs. Finally, the third heat-treatment step for selenization was conducted at 350 °C for 1 h in a 5% H_2/Ar atmosphere with Se powder. For comparison, bare $CoSe_2$-filled nanofibers (hereinafter denoted as bare $CoSe_2$-filled NF) without C were also prepared. $Co(CH_3COO)_2$-PVA composite fibers without GO and PS nanobeads prepared via electrospinning were heat-treated at 600 °C for 5 h in an air atmosphere. The resulting bare Co_3O_4 nanofibers were selenized at 500 °C for 6 h in a 5% H_2/Ar atmosphere to obtain the bare $CoSe_2$-filled NF.

Characterization: The morphological features of the nanofibers were investigated using FE-SEM (ULTRA PLUS, ZEISS) and field-emission TEM (JEOL, JEM-2100F). The crystal structures were investigated via XRD analysis (D8 Discover with GADDS, Bruker) using Cu K_α radiation (λ = 1.5418 Å). XPS was performed using a Thermo Scientific K-Alpha spectrometer with Al $K\alpha$ radiation to analyze the chemical compositions of the samples. A structural investigation of the C contents in the sample was performed using Raman spectroscopy (LabRam HR800, Horiba Jobin-Yvon, excited by a 515-nm diode laser at 25 °C). The surface areas of the samples were measured using the BET method, where N_2 was used as the adsorbate gas. TG analysis was performed using a Pyris 1 TGA (Perkin Elmer) in the temperature range of 25–700 °C at a heating rate of 10 °C min^{-1} in air.

Electrochemical Measurements: The electrochemical performance of the samples as anodes for SIBs was evaluated using 2032-type coin cells. The coin cells were assembled in a glovebox in an Ar atmosphere. The anode materials were prepared by casting 70 wt% active materials, 20 wt% carbon black (Super-P) as a conductive material, and 10 wt% sodium carboxymethyl cellulose as a binder in deionized water on Cu foil. Na metal and a microporous polypropylene film were used as the counter electrode and separator, respectively. In this study, two types of electrolytes were employed. First, a carbonate-based electrolyte comprising 1.0 м $NaClO_4$ in a mixture of EC and DMC (1:1 by volume) with 5 wt% fluoroethylene carbonate was used. The composites were cycled within the potential range of 0.001–3 V. Second, an ether-based electrolyte comprising 1.0 м sodium trifluoromethanesulfonate ($NaCF_3SO_3$) dissolved in DEGDME was used. The composites were cycled within the potential range of 0.3–2.9 V at various current densities to investigate the overall electrochemical behaviors of the electrodes. CVs were measured at a scan rate of 0.1 mV s^{-1}. The diameter of the negative electrode was 14 mm, and the specific capacities of cells were calculated based on the electrode mass loading (1.2 mg cm^{-2}). EIS was conducted in the frequency range of 100 kHz to 10 mHz using a perturbation of 10 mV.

Supporting Information

Supporting Information is available from the Wiley Online Library or from the author.

Acknowledgements

This work was supported by the National Research Foundation of Korea (NRF) grant funded by the Korea government (MSIP) (NRF-2018R1A4A1024691, NRF-2017M1A2A2087577, and NRF-2018R1D1A3B07042514).

Conflict of Interest

The authors declare no conflict of interest.

Keywords

anode materials, carbon nanotubes, cobalt selenide, graphene, sodium-ion batteries

Received: June 2, 2020
Revised: July 13, 2020

[1] Z. Hu, Q. Liu, S.-L. Chou, S.-X. Dou, *Adv. Mater.* **2017**, *29*, 1700606.
[2] Y. Lu, Y. Lu, Z. Niu, J. Chen, *Adv. Energy Mater.* **2018**, *8*, 1702469.
[3] C. Wu, S.-X. Dou, Y. Yu, *Small* **2018**, *14*, 1703671.
[4] Z. Liu, T. Lu, T. Song, X.-Y. Yu, X. W. D. Lou, U. Paik, *Energy Environ. Sci.* **2017**, *10*, 1576.
[5] J. S. Cho, H. S. Ju, J.-K. Lee, Y. C. Kang, *Nanoscale* **2017**, *9*, 1942.
[6] J. S. Cho, J. M. Won, J.-K. Lee, Y. C. Kang, *Nano Energy* **2016**, *26*, 466.
[7] S.-K. Park, J. K. Kim, Y. C. Kang, *Chem. Eng. J.* **2018**, *334*, 2440.
[8] S. H. Choi, Y. C. Kang, *Nanoscale* **2016**, *8*, 4209.
[9] Y. Ma, Y. Ma, D. Bresser, Y. Ji, D. Geiger, U. Kaiser, C. Streb, A. Varzi, S. Passerini, *ACS Nano* **2018**, *12*, 7220.
[10] S. Peng, X. Han, L. Li, Z. Zhu, F. Cheng, M. Srinivansan, S. Adams, S. Ramakrishna, *Small* **2016**, *12*, 1359.
[11] J. Ren, R.-P. Ren, Y.-K. Lv, *Chem. Eng. J.* **2018**, *353*, 419.
[12] C. Xu, Y. Jing, J. He, K. Zhou, Y. Chen, Q. Li, J. Lin, W. Zhang, *J. Alloy. Compd.* **2017**, *708*, 1178.
[13] C. Zhu, X. Mu, P. A. van Aken, J. Maier, Y. Yu, *Adv. Energy Mater.* **2015**, *5*, 1401170.
[14] Z.-J. Fan, J. Yan, T. Wei, G.-Q. Ning, L.-J. Zhi, J.-C. Liu, D.-X. Cao, G.-L. Wang, F. Wei, *ACS Nano* **2011**, *5*, 2787.
[15] E. Lee, K. A. Persson, *Nano Lett.* **2012**, *12*, 4624.
[16] X. Lu, H. Dou, B. Gao, C. Yuan, S. Yang, L. Hao, L. Shen, X. Zhang, *Electrochim. Acta* **2011**, *56*, 5115.
[17] L. Shen, X. Zhang, H. Li, C. Yuan, G. Cao, *J. Phys. Chem. Lett.* **2011**, *2*, 3096.
[18] Q. Su, Y. Liang, X. Feng, K. Müllen, *Chem. Commun.* **2010**, *46*, 8279.
[19] B. Zhang, Q. B. Zheng, Z. D. Huang, S. W. Oh, J. K. Kim, *Carbon* **2011**, *49*, 4524.
[20] Y. Wang, D. Kong, W. Shi, B. Liu, G. J. Sim, Q. Ge, H. Y. Yang, *Adv. Energy Mater.* **2016**, *6*, 1601057.
[21] J. Cui, S. Yao, Z. Lu, J.-Q. Huang, W. G. Chong, F. Ciucci, J.-K. Kim, *Adv. Energy Mater.* **2018**, *8*, 1702488.
[22] G. D. Park, J. H. Kim, S.-K. Park, Y. C. Kang, *ACS Appl. Mater. Interfaces* **2017**, *9*, 10673.
[23] M.-S. Balogun, Y. Luo, W. Qiu, P. Liu, Y. Tong, *Carbon* **2016**, *98*, 162.
[24] J. K. Kim, S. Y. Jeong, S. H. Lim, J. H. Oh, S.-K. Park, J. S. Cho, Y. C. Kang, *Chem. Asian J.* **2019**, *14*, 3127.
[25] C. H. Choi, S. H. Park, S. I. Woo, *Appl. Catal., B* **2012**, *119*, 123.
[26] J. Lee, J. H. Moon, *Korean J. Chem. Eng.* **2017**, *34*, 3195.
[27] F. T. Johra, J.-W. Lee, W.-G. Jung, *J. Ind. Eng. Chem.* **2014**, *20*, 2883.
[28] Y.-L. Ding, P. Kopold, K. Hahn, P. A. van Aken, J. Maier, Y. Yu, *Adv. Funct. Mater.* **2016**, *26*, 1112.
[29] S. K. Park, J.-K. Lee, Y. C. Kang, *Adv. Funct. Mater.* **2018**, *28*, 1705264.
[30] S.-K. Park, Y. C. Kang, *ACS Appl. Mater. Interfaces* **2018**, *10*, 17203.

[31] Y. Tang, Z. Zhao, X. Hao, Y. Wang, Y. Liu, Y. Hou, Q. Yang, X. Wang, J. Qiu, *J. Mater. Chem. A* **2017**, *5*, 13591.
[32] K. Zhou, J. He, X. Wang, J. Lin, Y. Jing, W. Zhang, Y. Chen, *Electrochim. Acta* **2017**, *231*, 626.
[33] C. Xia, Q. Jiang, C. Zhao, M. N. Hedhili, H. N. Alshareef, *Adv. Mater.* **2016**, *28*, 77.
[34] S.-K. Park, A. Jin, S.-H. Yu, J. Ha, B. Jang, S. Bong, S. Woo, Y.-E. Sung, Y. Piao, *Electrochim. Acta* **2014**, *120*, 452.
[35] Y.-C. Zhang, Y. You, S. Xin, Y.-X. Yin, J. Zhang, P. Wang, X.-S. Zheng, F.-F. Cao, Y.-G. Guo, *Nano Energy* **2016**, *25*, 120.
[36] Y. Lu, D. Li, C. Lyu, H. Liu, B. Liu, S. Lyu, T. Rosenau, D. Yang, *Appl. Surf. Sci.* **2019**, *496*, 143717.
[37] F. Niu, J. Yang, N. Wang, D. Zhang, W. Fan, J. Yang, Y. Qian, *Adv. Funct. Mater.* **2017**, *27*, 1700522.
[38] J. K. Kim, G. D. Park, J. H. Kim, S.-K. Park, Y. C. Kang, *Small* **2017**, *13*, 1700068.
[39] B. Gendensuren, C. He, E. S. Oh, *Korean J. Chem. Eng.* **2020**, *37*, 366.
[40] L. Liu, Y.-X. Yin, J.-Y. Li, S.-H. Wang, Y.-G. Guo, L.-J. Wan, *Adv. Mater.* **2018**, *30*, 1706216.
[41] G. Meng, Q. Yang, X. Wu, P. Wan, Y. Li, X. Lei, X. Sun, J. Liu, *Nano Energy* **2016**, *30*, 831.
[42] J. C. Groen, L. A. A. Peffer, J. Pérez-Ramírez, *Microporous Mesoporous Mater.* **2003**, *60*, 1.
[43] S.-K. Park, J. K. Kim, Y. C. Kang, *Chem. Eng. J.* **2017**, *328*, 546.
[44] H. Tabassum, C. Zhi, T. Hussain, T. Qiu, W. Aftab, R. Zou, *Adv. Energy Mater.* **2019**, *9*, 1901778.
[45] J. S. Cho, Y. J. Hong, Y. C. Kang, *ACS Nano* **2015**, *9*, 4026.
[46] Y. Xu, G. Jian, Y. Liu, Y. Zhu, M. R. Zachariah, C. Wang, *Nano Energy* **2014**, *3*, 26.
[47] J.-S. Park, S. Y. Jeong, K. M. Jeon, Y. C. Kang, J. S. Cho, *Chem. Eng. J.* **2018**, *339*, 97.
[48] Y.-E. Zhu, L. Yang, X. Zhou, F. Li, J. Wei, Z. Zhou, *J. Mater. Chem. A* **2017**, *5*, 9528.
[49] J. S. Cho, J.-K. Lee, Y. C. Kang, *Sci. Rep.* **2016**, *6*, 23699.
[50] Y. J. Jo, J. D. Lee, *Korean J. Chem. Eng.* **2019**, *36*, 1724.
[51] J.-Y. Hwang, S.-T. Myung, J.-H. Lee, A. Abouimrane, I. Belharouak, Y.-K. Sun, *Nano Energy* **2015**, *16*, 218.
[52] I. Moeez, H.-G. Jung, H.-D. Lim, K. Y. Chung, *ACS Appl. Mater. Interfaces* **2019**, *11*, 41394.
[53] Z. Hu, Z. Zhu, F. Cheng, K. Zhang, J. Wang, C. Chen, J. Chen, *Energy Environ. Sci.* **2015**, *8*, 1309.
[54] S. Y. Jeong, J. S. Cho, *Nanomaterials* **2019**, *9*, 1362.
[55] P. Ge, H. Hou, S. Li, L. Huang, X. Ji, *ACS Appl. Mater. Interfaces* **2018**, *10*, 14716.
[56] C. Cui, Z. Wei, G. Zhou, W. Wei, J. Ma, L. Chen, C. Li, *J. Mater. Chem. A* **2018**, *6*, 7088.
[57] Y. Fang, X. Y. Yu, X. W. Lou, *Adv. Mater.* **2018**, *30*, 1706668.
[58] H. Kim, K. Lim, G. Yoon, J.-H. Park, K. Ku, H.-D. Lim, E. Sung, K. Kang, *Adv. Energy Mater.* **2017**, *7*, 1700418.
[59] H. Kim, J. Hong, Y.-U. Park, J. Kim, I. Hwang, K. Kang, *Adv. Funct. Mater.* **2015**, *25*, 534.
[60] Z. Li, L. Yuan, Z. Yi, Y. Sun, Y. Liu, Y. Jiang, Y. Shen, Y. Xin, Z. Zhang, Y. Huang, *Adv. Energy Mater.* **2014**, *4*, 1301473.
[61] M. Mao, F. Yan, C. Cui, J. Ma, M. Zhang, T. Wang, C. Wang, *Nano Lett.* **2017**, *17*, 3830.
[62] S. Y. Jeong, S.-K. Park, Y. C. Kang, J. S. Cho, *Chem. Eng. J.* **2018**, *351*, 559.
[63] J. S. Cho, S. Y. Lee, J.-K. Lee, Y. C. Kang, *ACS Appl. Mater. Interfaces* **2016**, *8*, 21343.